Physics-informed neural networks for understanding shear migration of particles in viscous flow

Daihui Lu and Ivan C. Christov*

School of Mechanical Engineering, Purdue University, West Lafayette, Indiana 47907, USA

November 9, 2021

Abstract

We harness the physics-informed neural network (PINN) approach to extend the utility of phenomenological models for particle migration in shear flow. Specifically, we propose to constrain the neural network training via a model for the physics of shear-induced particle migration in suspensions. Then, we train the PINN against experimental data from the literature, showing that this approach provides both better fidelity to the experiments, and novel understanding of the relative roles of the hypothesized migration fluxes. We first verify the PINN approach for solving the inverse problem of radial particle migration in a non-Brownian suspension in an annular Couette flow. In this classical case, the PINN yields the same value (as reported in the literature) for the ratio of the two parameters of the empirical model. Next, we apply the PINN approach to analyze experiments on particle migration in both non-Brownian and Brownian suspensions in Poiseuille slot flow, for which a definitive calibration of the phenomenological migration model has been lacking. Using the PINN approach, we identify the unknown/empirical parameters in the physical model through the inverse solver capability of PINNs. Specifically, the values are significantly different from those for the Couette cell, highlighting an inconsistency in the literature that uses the latter value for Poiseuille flow. Importantly, the PINN results also show that the inferred values of the empirical model's parameters vary with the shear Péclet number and the particle bulk volume fraction of the suspension, instead of being constant as assumed in previous literature.

1 Introduction

Phillips et al. [1] proposed an insightful phenomenological model for the shear-induced migration of particles in a low-Reynolds-number flow [2]. Specifically, they posited that the distribution of particles, accounted for by the volume fraction $\phi(\boldsymbol{x}, t)$ of the fluid–particle suspension, obeys a conservation law [1, 3]:

$$\frac{D\phi}{Dt} = -\boldsymbol{\nabla} \cdot \boldsymbol{J}. \tag{1}$$

In Eq. (1), the material derivative of the left-hand side represents the unsteady transport of particles by a flow $\boldsymbol{u}$, while $\boldsymbol{J}$ on the right-hand side represents a spatial flux arising from the hydrodynamic interactions of particles. Consequently, Eq. (1) is often referred to as a *diffusive-flux model* in the literature. Phillips et al. [1] decomposed the flux as $\boldsymbol{J} = \boldsymbol{N}_c + \boldsymbol{N}_\eta + \boldsymbol{N}_B$, where they posited that $\boldsymbol{N}_c$, $\boldsymbol{N}_\eta$ and $\boldsymbol{N}_B$ represent the particle fluxes due to the variations in the particle collision frequency, the spatial variations of the viscosity of the suspension (due to the nonuniform particle distribution [2, 4]), and the spatial variations of the concentration (responsible for Brownian diffusion, by Fick's law), respectively. For unidirectional flows, $D\phi/Dt = \partial\phi/\partial t$ [3].

Specifically, Phillips et al. [1] proposed the following "constitutive laws" for the diffusive fluxes:

$$\boldsymbol{N}_c = -K_c a_p^2 \left(\phi^2 \boldsymbol{\nabla}\dot{\gamma} + \phi\dot{\gamma}\boldsymbol{\nabla}\phi \right), \tag{2a}$$

---

*Corresponding author. christov@purdue.edu; http://tmnt-lab.org.

$$\boldsymbol{N}_\eta = -K_\eta \dot{\gamma} \phi^2 \left(\frac{a_p^2}{\eta} \right) \frac{d\eta}{d\phi} \boldsymbol{\nabla} \phi, \tag{2b}$$

$$\boldsymbol{N}_B = -D \boldsymbol{\nabla} \phi, \tag{2c}$$

where K_c and K_η are *a priori* unknown constants of order unity, which are found from experimental data (by fitting/calibration). Therefore, Eq. (1), with the fluxes given in Eqs. (2), becomes a *parametrized partial differential equation* (PDE). Here, a_p is a particle's radius, D is its Brownian diffusivity (in principle, known from the Stokes–Einstein relation $D = k_B T / 6\pi \eta_s a_p$ with T being temperature and k_B being Boltzmann's constant), η is the non-constant dynamic viscosity of the suspension, which may depend on many parameters [5], η_s is the carrier Newtonian fluid's viscosity, and $\dot{\gamma}(\boldsymbol{x}, t)$ is the non-uniform shear rate in the flow. For a general flow field $\boldsymbol{u} = \boldsymbol{u}(\boldsymbol{x}, t)$, the shear rate is evaluated as the magnitude of the rate-of-strain tensor $\boldsymbol{E} = \frac{1}{2}(\boldsymbol{\nabla} \boldsymbol{u} + \boldsymbol{\nabla} \boldsymbol{u}^\top)$, i.e., $\dot{\gamma} = \sqrt{2\boldsymbol{E} : \boldsymbol{E}}$.

At steady state, $\partial(\cdot)/\partial t = 0$. Then, Eq. (1) can be integrated once in space over some domain $\mathcal{V}$, with the constant of integration set to zero by imposing a no-flux condition on the domain's boundary $\partial \mathcal{V}$. Therefore, the resulting governing physics equation at steady-state is

$$\boldsymbol{N}_c + \boldsymbol{N}_\eta + \boldsymbol{N}_B = \boldsymbol{0}, \tag{3}$$

which is a transport equation expressing the conservation of particles. Equation (3) also implies that if the initial particle volume fraction is such that $\int_{\mathcal{A}} \phi(\boldsymbol{x}, 0) \, d\boldsymbol{x} = \phi_b = const.$ across any cross-section $\mathcal{A}$, then $\int_{\mathcal{A}} \phi(\boldsymbol{x}, t) \, d\boldsymbol{x} = \phi_b$ for any $t > 0$. Additionally, the flow field $\boldsymbol{u}$ obeys the low-Reynolds-number (inertialess) flow momentum equation [1], which takes the form (using a more standard [6] sign convention and definition of $\boldsymbol{E}$ as above):

$$\boldsymbol{\nabla} \cdot \boldsymbol{\tau} = \boldsymbol{\nabla} p, \qquad \boldsymbol{\tau} = 2\eta \boldsymbol{E}, \qquad \eta = \eta_s \eta_r(\phi), \tag{4}$$

where η_r (dimensionless) is the contribution from the suspension to be introduced below, and $p(\boldsymbol{x})$ is the hydrodynamic pressure. We will consider only neutrally buoyant suspensions, and so body forces are neglected in Eq. (4). The velocity field is additionally incompressible, $\boldsymbol{\nabla} \cdot \boldsymbol{u} = 0$, but this relation is automatically satisfied by the unidirectional flows considered herein [6], so it is not a physical constraint that we need to enforce explicitly.

The fluid mechanics of particulate suspensions remains a frontier problem [7], and the diffusive-flux model of Phillips et al. [1] is not without its criticisms [3]. Nevertheless, although much more sophisticated models of suspensions exist [8, 9], including the suspension balance model [10–14], the two-fluid model [15], even direct numerical simulation [16], Eqs. (1)–(2) remain a popular model through which to study shear-induced particle migration in suspensions [17–19].

"Disentagling" the individual effects of shear-induced fluxes in Eq. (3) has been of particular interest in the suspensions literature [20]. (Note that although Merhi et al. [20] also included a fourth, "curvature-induced" flux in Eq. (3), its origin has been disputed by Bricker and Butler [21].) Machine learning is a viable approach toward processing experimental data to disentangle the relative strengths of the fluxes in Eq. (3). To this end, in Section 2, we apply the physics-informed neural network (PINN) approach of Raissi et al. [22] towards understanding particle migration in shear flow. Specifically, we propose to constrain the neural network using the model given by Eqs. (3) and (4). In Section 3, we validate this approach on the classical Couette cell experiments (and modeling) of Phillips et al. [1]. Then, in Section 4, we apply the PINN approach to the more challenging case of Poiseuille channel flow. In doing so, we re-interpret experiments on pressure-driven flows of both non-Brownian (Section 4.2) and Brownian (Section 4.3) suspensions, uncovering new aspects of the shear-induced migration model. Finally, conclusions are drawn in Section 5. Additional data pre-processing and verification details (regarding the PINN calculations) are provided in Appendices A and B, respectively.

2   PINN algorithm description and implementation

In recent years, with the explosive growth of available data, computing modalities, and requisite hardware resources, deep learning algorithms have been applied to a range of problems arising from computer science, physics and engineering fields [23], including in the field of fluid mechanics [24]. It has been suggested

that machine learning could "have influence closer to the principles of fluid mechanics, when [...] used in conjunction with human reasoning" [25, p. 4]. In this vein, *physics-informed machine learning* has emerged as an approach that "integrates seamlessly data and mathematical physics models, even in partially understood ... contexts" [26]. Specifically, Raissi et al. [22] developed a computational approach to couple machine learning with some underlying physics (human reasoning), which they termed *physics-informed neural networks* (PINNs). PINNs are a deep learning framework for solving problems involving PDEs by embedding (in a suitable sense) the physics into the neural network. Due to their versatility, PINNs have been applied to solve forward and inverse problems in fluid mechanics [27–32], solid mechanics [33, 34], material science [35, 36], and heat transfer [37], amongst many other applications. PINNs are appealing due to their standardized implementation. They use automatic differentiation [38] techniques to discretize the differential operators needed for the back-propagation problem, as well as the PDEs representing the physics [22, 39]. This approach makes PINNs mesh-free and, thus, easy to use for evaluating the PDE residual even from sparse experimental data sets ('observations'). Importantly, PINNs can determine unknown parameters in the physics embedded therein, even from incomplete (or partial) data sets, making PINNs useful for reduced-order model calibration.

In this paper, we use a PINN to solve the inverse problem of reduced-model determination for particle migration in suspensions. Given measurements of a velocity field $\boldsymbol{u}$ and a particle volume fraction profile ϕ, we seek to learn the unknown parameters K_c and K_η in the fluxes given in Eqs. (2). The governing physics equations are embedded into the PINN as shown in Fig. 1. We use two independent deep neural networks (DNNs), NN(u) and NN(ϕ), to approximate the velocity distribution and particle distribution, respectively. Both NNs are fully-connected and feed-forward, with multiple hidden layers each.

Suppose that the measured data is available on N (possibly random) sample points. The residuals of the fluid's conservation of momentum equation (4) and the suspension's particle transport equation (3) (suitably simplified for some given flow conditions and domain geometry) are evaluated from the approximated values of $\boldsymbol{u}$ and ϕ at these N collocation points. Then, combining the error between predictions and observations with the error in satisfying the physics from the residuals, along with any constraints, we formulate a loss function as:

$$\mathscr{L} = \underbrace{w_u \mathrm{MSE}_u + w_\phi \mathrm{MSE}_\phi}_{\text{training data}} + \underbrace{w_m \mathrm{MSE}_m + w_p \mathrm{MSE}_p}_{\text{physics}} + \underbrace{w_c \mathrm{MSE}_c}_{\text{constraints}}, \tag{5}$$

where, for example,

$$\mathrm{MSE}_u = \frac{1}{N} \sum_{i=1}^{N} \|\boldsymbol{u}(i) - \boldsymbol{u}_{\text{train}}(i)\|^2, \tag{6a}$$

$$\mathrm{MSE}_\phi = \frac{1}{N} \sum_{i=1}^{N} |\phi(i) - \phi_{\text{train}}(i)|^2, \tag{6b}$$

$$\mathrm{MSE}_m = \frac{1}{N} \sum_{i=1}^{N} \|\boldsymbol{\nabla} \cdot \boldsymbol{\tau}(i) - \boldsymbol{\nabla} p(i)\|^2, \tag{6c}$$

$$\mathrm{MSE}_p = \frac{1}{N} \sum_{i=1}^{N} \|\boldsymbol{N}_c(i) + \boldsymbol{N}_\eta(i) + \boldsymbol{N}_B(i)\|^2. \tag{6d}$$

The MSE terms in $\mathscr{L}$ represent various "mean squared errors." The notation "(i)" denotes the value of the quantity at the ith data point in the set of N observations. For clarity, we omit this explicit notation below without fear of confusion. The first two terms of $\mathscr{L}$ correspond to the errors between the predicted and the input velocity and particle distribution training data, respectively. Then, the following two terms of $\mathscr{L}$ correspond to error in satisfaction of the physics, *i.e.*, the suspension's momentum equation (4) and particle transport equation (3), respectively. The last term of $\mathscr{L}$ represents error committed in satisfaction of "constraints." The constraints can involve, *e.g.*, boundary conditions, integral constraints, or any other mathematical statement not captured in the "physics" term, which is typically used to denote only the satisfaction of governing (partial) differential equations. The coefficients w_j where $j \in \{u, \phi, s, m, c\}$, represent weights of the corresponding loss terms. Although the relative values of the weights of terms in the loss function may influence the ability to train the NN [40], here we generally take them to be equal.
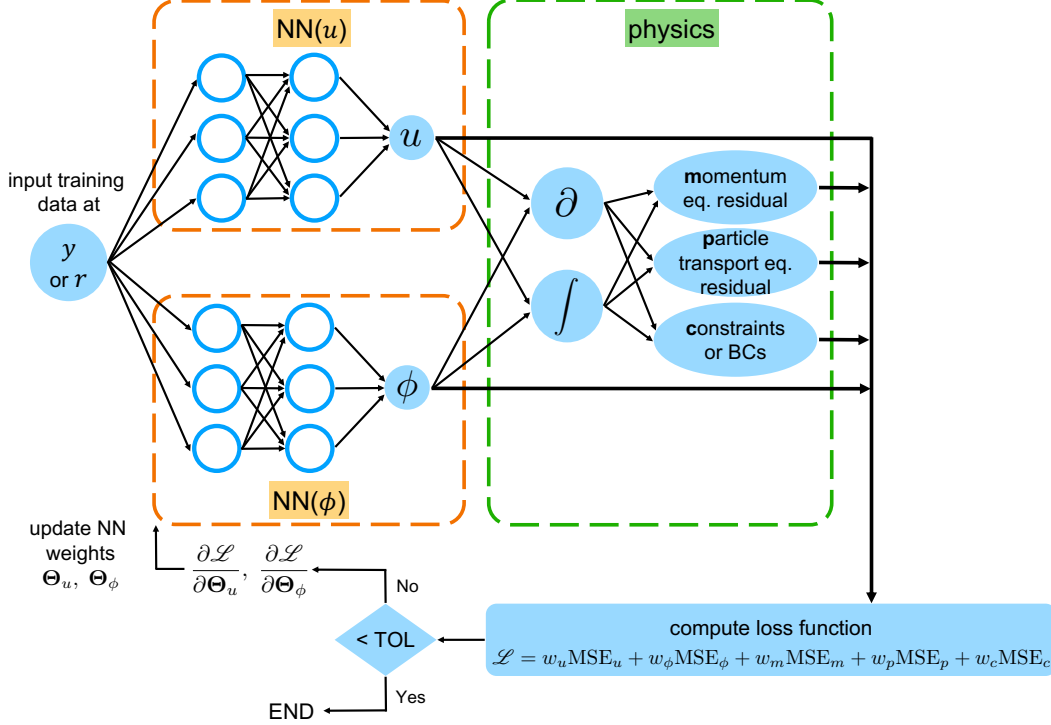
Figure 1: Architecture of the proposed PINN for solving the inverse problem of reduced-model determination for particle migration in suspensions. The loss $\mathscr{L}$ is formulated (as in Eq. (5)) in terms of root-mean-squared errors between predictions and observations (MSE_u, MSE_ϕ), and errors in satisfaction (residuals) of the underlying PDEs from the physics (MSE_m, MSE_p), as well as boundary conditions and/or additional constraints (MSE_c).

Figure 1 shows the architecture of the PINN for the case in which only a component u of the velocity vector $\boldsymbol{u}$ has been measured. Initially, a randomly selected set of network weight vectors $\boldsymbol{\Theta}_u^{(0)}$ and $\boldsymbol{\Theta}_\phi^{(0)}$ are used to construct $\text{NN}(u)$ and $\text{NN}(\phi)$, respectively. Then, we feed training data into $\text{NN}(u)$ and $\text{NN}(\phi)$ to obtain predictions on u and ϕ. We calculate the derivatives of u and ϕ needed to evaluate the physics-informed loss terms via automatic differentiation in TensorFlow [41]. Then, starting with guesses $K_c^{(0)}$ and $K_\eta^{(0)}$ for the model parameters, we calculate the loss terms corresponding to the particle transport and momentum equations, as well as any constraints. During the process of minimizing $\mathscr{L}$, $\boldsymbol{\Theta}_u^{(k)}$, $\boldsymbol{\Theta}_\phi^{(k)}$, $K_c^{(k)}$ and $K_\eta^{(k)}$ are updated at each iteration k. The loss function is minimized using "Adam" [42], which is a stochastic gradient descent algorithm. The stopping criterion for the optimization is that the change in the loss function between iterations is less than machine precision. However, this stopping criterion may or may not satisfy our convergence criterion. So, upon the stoppage of the optimization procedure, we check that $\mathscr{L} < \text{TOL}$, for some prescribed tolerance $\text{TOL} \simeq 10^{-2}$. Upon satisfaction of the latter criterion, we consider the solution converged. Then, we have obtained not only the optimized DNNs' weights $\boldsymbol{\Theta}_u$ and $\boldsymbol{\Theta}_\phi$, but also the initially unknown model parameters K_c and K_η.

3 Couette flow

3.1 Governing physics equations

For flow between concentric rotating cylinders, the domain is $\mathcal{V} = \{\boldsymbol{x} = (r, \theta) \mid \kappa R \leq r \leq R, \ 0 \leq \theta < 2\pi\}$, where $\kappa < 1$ is dimensionless, and the problem is independent of the axial, z, coordinate. The unidirectional velocity field is thus $\boldsymbol{u} = u_\theta(r)\boldsymbol{e}_\theta$. The radial component of the momentum equation (4) (now in cylindrical

coordinates [6]) reduces to

$$\frac{1}{r^2}\frac{\partial}{\partial r}\left(r^2\tau_{r\theta}\right)=0 \qquad \Rightarrow \qquad \tau_{r\theta}=\frac{A}{r^2}, \tag{7}$$

where A is a constant to be calculated by imposing boundary conditions [1]. Note that in this case of axisymmetric flow, $\partial p/\partial\theta = 0$. Equivalently,

$$\dot{\gamma}=\dot{\gamma}_{r\theta}=\frac{A}{r^2\eta}, \qquad A=\frac{-\Omega}{\int_{\kappa R}^{R}(r^3\eta)^{-1}\,dr}, \tag{8}$$

where Ω is the angular velocity of the inner cylinder. On dimensional grounds alone, for a neutrally buoyant non-Brownian suspension at low Reynolds number at steady state, it is expected that $\eta/\eta_s = \eta_r(\phi)$ [5], where η_s is the Newtonian solvent's dynamic viscosity, and $\eta_r(\phi)$ is the dimensionless contribution to the viscosity due to particles. Indeed, the experiments of Phillips et al. [1] were verified to be in this specific regime, and they used the empirical Krieger–Dougherty relation:

$$\eta_r(\phi)=\left(1-\frac{\phi}{\phi_m}\right)^{-a}, \tag{9}$$

where $\phi_m = 0.68$ is the maximum packing volume fraction, and $a = 1.82$ is a positive empirical exponent (in principle, related to ϕ_m [5]). The form of Eq. (9) and values for ϕ_m and a are based on experimental correlations [43, 44], and they are well-established for non-Brownian suspensions [9, 45]. Here, we are only interested in interrogating the particle migration model, so any fitting parameters for the fluid and suspension properties are taken as per the literature.

Next, dimensionless governing equations are obtained by scaling the dimensional variables in the following way:

$$r^* = r/R, \qquad \dot{\gamma}^*(r^*)=\dot{\gamma}_{r\theta}(r)/\Omega, \qquad u^*(r^*)=u_\theta(r)/U_{\max}, \tag{10}$$

where $U_{\max} = \Omega\kappa R$ is the maximum velocity at the rotating wall. Therefore, the momentum equation (8) can be written as

$$\dot{\gamma}^*(r^*)=\frac{-1}{r^{*2}\eta_r\int_\kappa^1(r^{*3}\eta_r)^{-1}\,dr^*}. \tag{11}$$

Neglecting the Brownian flux, the corresponding dimensionless particle transport equation (3) for the non-Brownian suspension in this geometry is

$$\frac{1}{\dot{\gamma}^*}\frac{d\dot{\gamma}^*}{dr^*}+\frac{1}{\phi}\frac{d\phi}{dr^*}+\frac{K_\eta}{K_c}\frac{1}{\eta_r}\frac{d\eta_r}{dr^*}=0. \tag{12}$$

Observe that in this (non-Brownian) case, only the ratio K_η/K_c of the two model parameters shows up in the final form of the particle transport equation. In other words, there is only a single quantity to "fit," and this fact is reflected in the PINN architecture used for this problem.

Additionally, the particle distribution satisfies

$$\frac{1}{1-\kappa}\int_\kappa^1\phi(r^*)\,dr^*=\phi_b, \tag{13}$$

where ϕ_b is the bulk volume fraction. The uniform distribution of particles at the initial time is then $\phi(r, t = 0) = \phi_b$, and at steady state conservation of mass requires that Eq. (13) hold.

Phillips et al. [1] suggested, based on analysis of their experiments, that $K_c/K_\eta \approx 0.66$ best fits the profile measured for steady-state Couette flow of suspensions of $2a_p = 675$ μm particles at $\phi_b = 0.55$. The agreement was also good when comparing with experimental data at $\phi_b = 0.45$, 0.50 and 0.55. In this section, we wish to investigate the best-fit value of K_c/K_η obtained by the PINN approach for solving the inverse problem.

3.2   PINN loss function

For this problem, the loss function is

$$\mathcal{L} = w_u \text{MSE}_u + w_\phi \text{MSE}_\phi + w_p \text{MSE}_p + w_m \text{MSE}_m + w_c \text{MSE}_c. \tag{14}$$

The notation for the MSE terms was introduced in Sec. 2. These terms are now implemented as

$$\text{MSE}_u = \frac{1}{N} \sum_{i=1}^{N} |u^* - u_{\text{train}}^*|^2, \tag{15a}$$

$$\text{MSE}_\phi = \frac{1}{N} \sum_{i=1}^{N} |\phi - \phi_{\text{train}}|^2, \tag{15b}$$

$$\text{MSE}_m = \frac{1}{N} \sum_{i=1}^{N} \left| \dot{\gamma}^* + \frac{1}{r^{*2} \eta_r \int_\kappa^1 (r^{*3} \eta_r)^{-1} dr^*} \right|^2, \tag{15c}$$

$$\text{MSE}_p = \frac{1}{N} \sum_{i=1}^{N} \left| \frac{1}{\dot{\gamma}^*} \frac{d\dot{\gamma}^*}{dr^*} + \frac{1}{\phi} \frac{d\phi}{dr^*} + \frac{K_\eta}{K_c} \frac{1}{\eta_r} \frac{d\eta_r}{dr^*} \right|^2, \tag{15d}$$

$$\text{MSE}_c = \left| \frac{1}{1-\kappa} \int_\kappa^1 \phi(r^*) \, dr^* - \phi_b \right|^2. \tag{15e}$$

The integrals in the expressions in Eqs. (15c) and (15e) are approximated by averages over the randomly selected set of collocation points (essentially a Monte Carlo quadrature): $\int_\kappa^1 (\cdot) = \sum_{i=1}^{N} (\cdot) \times (1-\kappa)/N$. Appendix A describes how the experimental data (digitized from [1]) was pre-processed into training data.

Note that the output variables of the NNs are u and ϕ, as depicted in Fig. 1. Thus, the remaining variables η_r and $\dot{\gamma}^*$ have to be expressed in terms of these output variables. Recall that $\dot{\gamma} = r d(u_\theta/r)/dr$ for purely azimuthal flow by definition [6]. Then, using the nondimensionalization from Eq. (10):

$$\dot{\gamma}^*(r^*) = \kappa r^* \frac{d}{dr^*} \left(\frac{u^*(r^*)}{r^*} \right). \tag{16}$$

Substituting the expression for $\dot{\gamma}^*$ from Eq. (16) and η_r from Eq. (9) into the MSE expressions (15c) and (15d), the loss function from Eq. (14) now depends only on the DNNs' weights ($\boldsymbol{\Theta}_u$ and $\boldsymbol{\Theta}_\phi$) and the parameter K_c/K_η. By minimizing the resulting $\mathcal{L}(\boldsymbol{\Theta}_u, \boldsymbol{\Theta}_\phi, K_c/K_\eta)$ with respect to its arguments, we obtain NN(u), NN(ϕ), and the value of K_c/K_η that simultaneously lead to the best agreement with the training data *and* the physics.

3.3   Comparison between PINN, theory and experiment

To evaluate the "theoretical" particle distribution profile, we use $d\eta_r/dr^* = (d\eta_r/d\phi)(d\phi/dr^*)$ to re-write Eq. (12) as:

$$\left(\frac{1}{\phi} + \frac{K_\eta}{K_c} \frac{1}{\eta_r} \frac{d\eta_r}{d\phi} \right) \frac{d\phi}{dr^*} = -\frac{1}{\dot{\gamma}^*} \frac{d\dot{\gamma}^*}{dr^*} = \left(\frac{2}{r^*} + \frac{1}{\eta_r} \frac{d\eta_r}{d\phi} \frac{d\phi}{dr^*} \right), \tag{17}$$

where the second equality follows from using the dimensionless version of Eq. (8). Now, Eq. (17) can be rearranged as an ODE for $\phi(r^*)$:

$$\left[\frac{1}{\phi} + \left(\frac{K_\eta}{K_c} - 1 \right) \frac{1}{\eta_r} \frac{d\eta_r}{d\phi} \right] \frac{d\phi}{dr^*} = \frac{2}{r^*}. \tag{18}$$

Finally, we can use the Krieger viscosity from Eq. (9), multiply both sides of Eq. (18) by ϕ and solve for $d\phi/dr^*$, to obtain a first-order nonlinear ODE for $\phi(r^*)$:

$$\frac{d\phi}{dr^*} = \frac{2\phi}{[(K_\eta/K_c - 1)a(\phi/\phi_m)(1 - \phi/\phi_m)^{-1} + 1]r^*}, \tag{19}$$
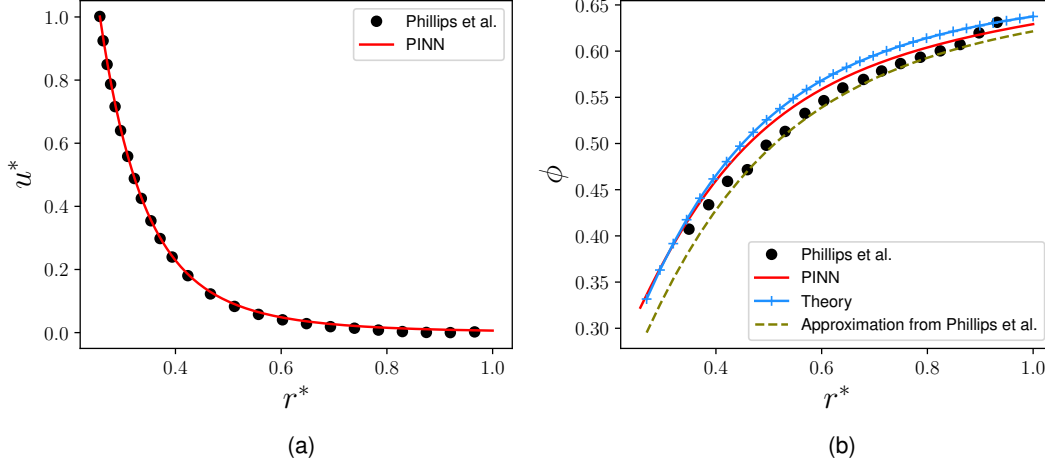
Figure 2: Validation of the proposed PINN approach to shear-induced migration. The PINN is applied to analyze the experiment from Phillips et al. [1] in a concentric Couette cell at $\phi_b = 0.55$, yielding: (a) the dimensionless velocity profile $u^*(r^*)$ and (b) the particle distribution (volume fraction) $\phi(r^*)$. Symbols represent the experimental data from Phillips et al. [1]; red solid curves are PINN predictions; curve with cross symbols is the numerical solution of Eq. (19); dashed curve in (b) is the approximate analytical solution from Phillips et al. [1, Eqs. (24)–(25)]. The PINN "learns" a value of the unknown model parameter $K_c/K_\eta \approx 0.66$, which is in agreement with [1].

which is the same as Eq. (21) of Phillips et al. [1]. Equation (19) can be integrated from $r^* = \kappa$ to $r^* = 1$ using an arbitrary value $\phi(r^* = \kappa) = \phi_w \in [0, 1]$ as the initial condition. Then, a nonlinear iteration (implemented using `optimize.root_scalar` from the SciPy stack in Python [46]) updates ϕ_w until the constrain (13) is satisfied for the given ϕ_b. This solution will be shown as the "theory" curve in the figures below.

In Fig. 2, we compare our PINN results using $w_u = w_\phi = w_m = w_p = w_c = 1$ to theory (numerical solution of Eq. (19)) and the experiments (by Phillips et al. [1]). We use DNNs with two hidden layers with 10 nodes in each layer and a learning rate of 0.001 for the Adam optimizer. The process of choosing a suitable number of layers and nodes is discussed in Appendix B.

Two versions of the theoretical prediction for the particle distribution profile are shown in Fig. 2(b). One is calculated by solving Eq. (19) (numerically by the method described above) using the value $K_c/K_\eta = 0.66$ suggested in [1]. The other theoretical prediction is derived via the *ad-hoc* approximation $1.82(1 - K_\eta/K_c) \approx -1$ made in Phillips et al. [1]. We observe that the PINN prediction is an improvement over the numerical solution of Eq. (19). Surprisingly, the approximation $1.82(1 - K_\eta/K_c) \approx -1$ improves the agreement further between the theory and experiments. This approximation, made out of convenience in [1], does not appear to be justifiable on the basis of mathematical grounds (such as perturbation theory), therefore its good agreement with experiment must be simply coincidence.

As evidenced by Fig. 2, we obtain good agreement between the PINN predictions and the experimental data, for both u^* and ϕ. To account for the statistical variation in the converged ("learned") value of K_c/K_η due to the random initialization of the NNs, we averaged the predictions from 100 using different initializations to obtain a statistical result with mean and standard error: $K_c/K_\eta = 0.66 \pm 0.05$, which is consistent with the fitted value in [1] by their non-machine-learning approach. Thus, we have validated the PINN approach for the shear-induced migration of non-Brownian particles in a concentric Couette cell, showing that PINNs not only provide suitable predictions for the velocity and particle distribution profiles, but they also "learn" the accepted value of the model parameter K_c/K_η given in the literature.

4   Poiseuille flow

4.1   Governing physics equations

For Poiseuille flow in a slot of height $2H$, the domain is $\mathcal{V} = \{\boldsymbol{x} = (x, y) \mid -H \leq y \leq +H, \; -\infty < x < \infty\}$. For fully developed flow, the x dependence drops out. The unidirectional velocity field is thus $\boldsymbol{u} = u_z(y)\boldsymbol{e}_z$. We introduce the dimensionless variables

$$x^* = x/L, \qquad y^* = y/H, \qquad \dot{\gamma}^*(y^*) = \dot{\gamma}(y)/\dot{\gamma}_0, \qquad u^*(y^*) = u_z(y)/U_{\max}, \tag{20}$$

where $U_{\max}$ is the centerline (maximum) velocity of the solvent fluid at the same volumetric flow rate, $\dot{\gamma}_0 = U_{\max}/H$ is the mean shear rate, and L is a typical axial length scale for the channel.

Now, the dimensionless particle transport equation (3) for the suspension takes the form

$$K_c \phi \left(\phi \frac{d^2 u^*}{dy^{*2}} + \frac{du^*}{dy^*} \frac{d\phi}{dy^*} \right) + K_\eta \frac{du^*}{dy^*} \frac{\phi^2}{\eta_r} \frac{d\eta_r}{dy^*} + \frac{1}{Pe} \frac{d\phi}{dy^*} = 0. \tag{21}$$

In Eq. (21), Pe is the shear Péclet number, which quantifies the relative importance of shear migration to Brownian migration of particles [5], defined as

$$Pe = \frac{a_p^2 \dot{\gamma}_0}{D} = \frac{6\pi \eta_s a_p^3 \dot{\gamma}_0}{k_B T}, \tag{22}$$

where k_B is Boltzmann's constant, and T is temperature. Observe that unlike the case of Eq. (12), Eq. (21) for finite Pe cannot be divided by K_c (to only consider the ratio K_η/K_c). Again, the particle distribution is constrained such that

$$\frac{1}{2} \int_{-1}^{+1} \phi(y^*) \, dy^* = \int_0^1 \phi(y^*) \, dy^* = \phi_b. \tag{23}$$

For a dense non-Brownian suspension ($Pe \gg 1$), the velocity is not parabolic [1, 47]. Its shape is found by solving the momentum equation (4) for pressure-driven Poiseuille flow of the suspension:

$$\frac{d}{dy^*} \left(\eta_r(\phi) \frac{du^*}{dy^*} \right) = G^* = \frac{GH^2}{\eta_s U_{\max}}, \tag{24}$$

where G^* (resp. G) is the dimensionless (resp. dimensional) axial pressure gradient, which is constant in unidirectional flow [6]. Integrating Eq. (24) once and imposing a centerline symmetry condition, we have

$$\eta_r(\phi) \frac{du^*}{dy^*} = G^* y^*. \tag{25}$$

Similarly to the approach of Reyes et al. [31], Eq. (25) will be enforced via the PINN's loss function to account for the blunted (non-parabolic) velocity profiles of dense suspensions. However, we will not enforce no-slip boundary conditions with Eq. (25) because experiments [47–49] suggest that dense suspensions can slip along the channel walls (see Fig. 3). The proposed machine learning methodology naturally handles slip without further effort.

For a strongly Brownian suspension ($Pe = \mathcal{O}(1)$), as we will discuss in Sec. 4.3, the velocity profile in experiments [50] is indistinguishable from a parabolic one, so instead of Eq. (25), we can simply enforce

$$u^*(y^*) = 1 - y^{*2}. \tag{26}$$

In this way, we do not need to know the value of G, which is not always available in the published experimental papers. (Put differently: $\eta_r(\phi) \approx 1$ and the scale $U_{\max}$ is chosen to make $G^* = 1$ in this case.)

4.2   Non-Brownian dense suspension

4.2.1   PINN loss function

In a non-Brownian dense suspension, the Brownian diffusive flux $\boldsymbol{N}_B$ can be neglected in Eq. (3), which eliminates the term $Pe^{-1}d\phi/dy^*$ from Eq. (21) (equivalently, the limit $Pe \to \infty$ corresponds to a non-Brownian suspension). Then, in this case, the MSE terms as introduced in Eq. (5) in Sec. 2 are now be implemented as:

$$\text{MSE}_u = \frac{1}{N}\sum_{i=1}^{N}|u^* - u^*_{\text{train}}|^2, \tag{27a}$$

$$\text{MSE}_\phi = \frac{1}{N}\sum_{i=1}^{N}|\phi - \phi_{\text{train}}|^2, \tag{27b}$$

$$\text{MSE}_m = \frac{1}{N}\sum_{i=1}^{N}\left|\eta_r(\phi)\frac{du^*}{dy^*} - G^*y^*\right|^2, \tag{27c}$$

$$\text{MSE}_p = \frac{1}{N}\sum_{i=1}^{N}\left|\frac{K_c}{K_\eta}\phi\left(\phi\frac{d^2u^*}{dy^{*2}} + \frac{du^*}{dy^*}\frac{d\phi}{dy^*}\right) + \frac{du^*}{dy^*}\frac{\phi^2}{\eta_r}\frac{d\eta_r}{dy^*}\right|^2, \tag{27d}$$

$$\text{MSE}_c = \left|\int_0^1 \phi(y^*)dy^* - \phi_b\right|^2. \tag{27e}$$

Appendix A describes how the experimental data (digitized from [47]) was pre-processed into training data.

Note that in MSE_p, $d\eta_r/dy^*$ is calculated by the chain rule: $d\eta_r/dy^* = (d\eta_r/d\phi)(d\phi/dy^*)$. Then, substituting η_r from Eq. (9) into the loss function, we obtain $\mathscr{L}$, which depends only on the DNNs' weights ($\boldsymbol{\Theta}_u$ and $\boldsymbol{\Theta}_\phi$) and the ratio K_c/K_η. By minimizing the resulting $\mathscr{L}(\boldsymbol{\Theta}_u, \boldsymbol{\Theta}_\phi, K_c/K_\eta)$ with respect to its arguments using $w_u = w_\phi = w_m = w_p = w_c = 1$, we find suitable DNNs' weights and the value of the parameter K_c/K_η that simultaneously leads to the best agreement with the training data *and* the physics.

4.2.2   Comparison between PINN, theory and experiment

We can solve for the "theoretical" prediction for ϕ from Eq. (21). For a non-Brownian suspensions, the dependence of the viscosity on the particle volume fraction is given by Eq. (9), and the velocity profile obeys Eqs. (25). Substituting these expressions into Eq. (21) and neglecting the Brownian term ($Pe \to \infty$), we once again obtain a nonlinear first-order ODE for $\phi(y^*)$:

$$\frac{d\phi}{dy^*} = \frac{\phi}{\left[(1 - K_\eta/K_c)\, a(\phi/\phi_m)\left(1 - \phi/\phi_m\right)^{-1} - 1\right]y^*}, \tag{28}$$

Then, Eq. (28) can be integrated numerically from $y^* = 1$ back to $y^* = 0$ (to handle the singularity at $y^* = 0$). An arbitrary value $\phi(y^* = 1) = \phi_w \in [0,1]$ is used as an initial guess. Then, a nonlinear iteration (implemented using `optimize.root_scalar` from the SciPy stack in Python [46]) updates ϕ_w until the constrain (23) is satisfied for the given ϕ_b. This solution will be shown as the "theory" curve in the figures below. Note that, while Koh et al. [47] assumed $K_c/K_\eta = 0.66$ (based on the result in Sec. 3.3), we use the value of K_c/K_η learned by the PINN instead.

In Fig. 3, 4, 5 we compare the PINN solutions to the laser-Doppler velocimetry experimental measurements of Koh et al. [47] at $\phi_b = 0.1, 0.2, 0.3$, respectively. As in Sec. 3.1, we use the scaled viscosity function $\eta_r(\phi)$ given in Eq. (9), because their experiments are also for a neutrally buoyant non-Brownian suspension at low Reynolds number, like [1]. As can be deduced from the figures, the PINN predictions for the profiles $u^*(y^*)$ and $\phi(y^*)$ agree well with the experiment data. Specifically, the PINN predicts ϕ better than pure theory from Eq. (28) because, when using Eq. (28) as a constraint on the learning process, the PINN "smooths out" the physically-questionable singularity of the ODE at $y^* = 0$. Note that this feature of the PINN approach was also mentioned in [31], in the context of the shear stress singularity at the channel centerline under a power-law rheological model.
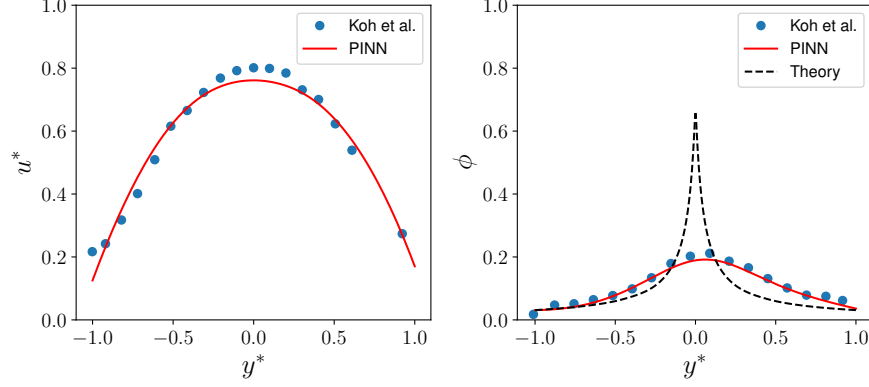
Figure 3: Application of the proposed PINN-based approach for understanding shear-induced migration to experiment 187 from Koh et al. [47] at $\phi_b = 0.1$. The PINN found $K_c/K_\eta = 0.10 \pm 0.012$.
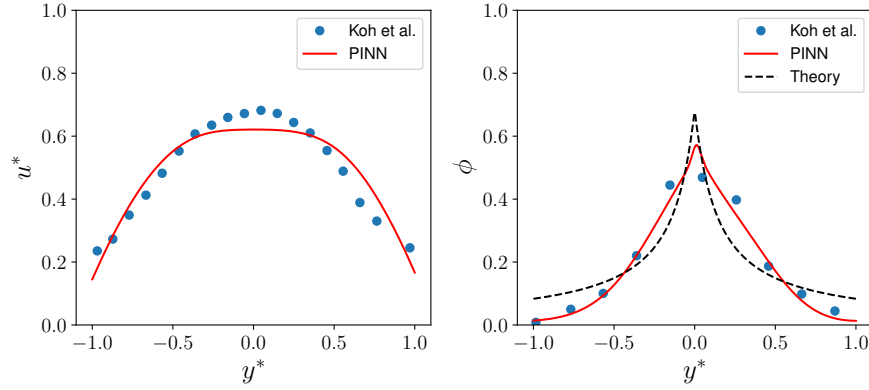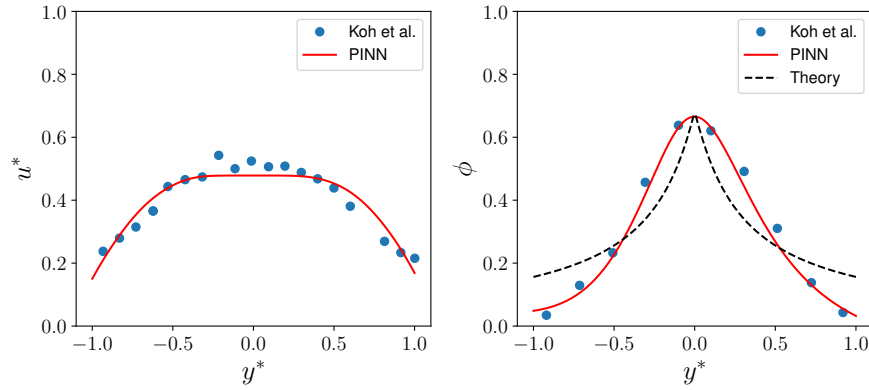

Figure 4: Application of the proposed PINN-based approach for understanding shear-induced migration to experiment 189 from Koh et al. [47] at $\phi_b = 0.2$. The PINN found $K_c/K_\eta = 0.44 \pm 0.018$.

Figure 5: Application of the proposed PINN-based approach for understanding shear-induced migration to experiment 192 from Koh et al. [47] at $\phi_b = 0.3$. The PINN found $K_c/K_\eta = 0.58 \pm 0.020$.

Importantly, by training the PINN, we deduce best-fit K_c/K_η values *different* from the traditional value of 0.66, which has only been validated for the concentric Couette flow (Sec. 3.3). Table 1 summarizes the values that the PINN "learns" from experimental data with different values of ϕ_b for the Poiseuille flow in a slot.

ϕ_b	K_c/K_η
0.1	0.10 ± 0.012
0.2	0.44 ± 0.018
0.3	0.58 ± 0.020

Table 1: Values of the shear-induced migration model's parameter K_c/K_η, as inferred by the PINN from non-Brownian experimental data of Koh et al. [47], for different bulk volume fractions ϕ_b. As before, these statistical results, with a mean and a standard error, come from 100 runs of the PINN algorithm using different random initializations of the NNs.

4.3 Brownian suspension

Now, we return to the "full" Eq. (21) at finite Pe, which was defined in Eq. (22). Now, it is expected that $\eta/\eta_s = \eta_r(\phi, Pe)$ [5] (see also [9, Ch. 7]), while the suspension is still neutrally buoyant, at steady state and at low Reynolds number. (The geometry is still that of Poiseuille flow in a slot as introduced in Sec. 4.2.)

Unlike the previous sections, we can no longer use the Krieger–Dougherty viscosity function from Eq. (9) for the Brownian suspension. Instead, motivated by the work of Kang and Mirbod [17], we take the Brownian suspension's shear viscosity to be

$$\eta_r(\phi, Pe) = \eta_\infty(\phi) + \frac{\eta_0(\phi) - \eta_\infty(\phi)}{1 + K_{Pe}\eta_s a_p^3 \dot{\gamma}/(k_B T)} = \eta_\infty(\phi) + \frac{\eta_0(\phi) - \eta_\infty(\phi)}{1 + K_{Pe}Pe\dot{\gamma}^*/(6\pi)}, \tag{29}$$

where

$$\eta_0(\phi) = (1 - \phi/\phi_{m_0})^{-\mathfrak{a}_0}, \tag{30a}$$

$$\eta_\infty(\phi) = (1 - \phi/\phi_{m_\infty})^{-\mathfrak{a}_\infty}, \tag{30b}$$

based on the correlations proposed by de Kruif et al. [51]. Typically, $\phi_{m_0} = 0.63$, $\phi_{m_\infty} = 0.71$, $\mathfrak{a}_0 = 1.96$, $\mathfrak{a}_\infty = 1.93$, and $K_{Pe} = 1.31$ are used in the literature [17] based on experimental fits. While the zero-Pe and infinite-Pe "plateaus" of the viscosity function (29) can be measured accurately (yielding the maximum volume fractions ϕ_{m_0} and ϕ_{m_∞}, along with the exponents $\mathfrak{a}_0$ and $\mathfrak{a}_\infty$), the transition over intermediate Pe is characterized by the dimensionless parameter K_{Pe}. This parameter is harder to infer from a single experiment (and, indeed, has *not* been reported in the papers on shear-induced migration of Brownian particles), thus we propose to treat it as *a priori* unknown, like K_c and K_η. In other words, we will self-consistently determine the unknown K_{Pe} via the inverse formulation in the PINN approach applied to experiments of Frank et al. [50] on shear-induced migration of colloidal particles.

Observe that we keep the variable local shear rate $\dot{\gamma}^* = \dot{\gamma}^*(y^*) = du^*/dy^*$ (dimensionless, recall Eq. (20)) in Eq. (29) because $\dot{\gamma}^* \neq const.$ in Poiseuille flow. Nevertheless, using particle-image velocimetry, Frank et al. [50] found experimentally that the velocity profile of their Brownian suspension (of $2a_p = 2$ μm spherical colloidal particles) flowing through a rectangular channel only slightly deviates from the parabolic profile of the solvent (see Fig. 6), hence $\dot{\gamma}^*(y^*) \approx -2y^*$. Therefore, for the Brownian suspensions, we shall use the parabolic profile from Eq. (26) to define MSE_m in the loss function, instead of the full momentum equation.

4.3.1 PINN loss function

For the Brownian suspension, the MSE terms is as introduced in Eq. (5) in Sec. 2 are now implemented as:

$$\mathrm{MSE}_u = \frac{1}{N} \sum_{i=1}^{N} |u^* - u^*_{\mathrm{train}}|^2, \tag{31a}$$

$$\mathrm{MSE}_\phi = \frac{1}{N} \sum_{i=1}^{N} |\phi - \phi_{\mathrm{train}}|^2, \tag{31b}$$

$$\mathrm{MSE}_m = \frac{1}{N} \sum_{i=1}^{N} \left|u^* - 1 + y^{*2}\right|^2, \tag{31c}$$
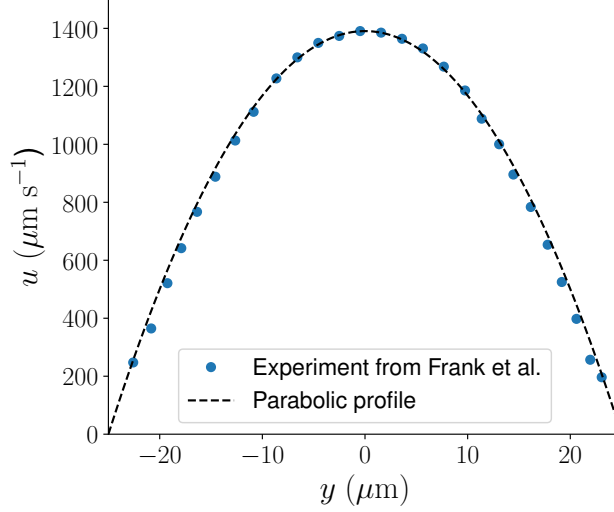
Figure 6: Measured axial velocity of a Brownian suspension in Poiseuille flow reproduced from Frank et al. [50] is compared to a dimensional version of the parabolic profile from Eq. (26), showing good agreement. The channel width is $2H = 50$ µm, and $U_{\max} \approx 1391$ µm s^{-1} from the figure in [50].

$$\mathrm{MSE}_p = \frac{1}{N} \sum_{i=1}^{N} \left| K_c \phi \left(\phi \frac{d^2 u^*}{dy^{*2}} + \frac{du^*}{dy^*} \frac{d\phi}{dy^*} \right) + K_\eta \frac{du^*}{dy^*} \frac{\phi^2}{\eta_r} \frac{d\eta_r}{dy^*} + \frac{1}{Pe} \frac{d\phi}{dy^*} \right|^2, \tag{31d}$$

$$\mathrm{MSE}_c = \left| \int_0^1 \phi(y^*) \, dy^* - \phi_b \right|^2. \tag{31e}$$

Appendix A describes how the experimental data (digitized from [50]) was pre-processed into training data.

Using η_r from Eq. (29), we can calculate $d\eta_r/dy^* = (d\eta_r/d\phi)(d\phi/dy^*)$ in Eq. (31d) by the chain rule. Now, the loss $\mathscr{L}$ (recall Eq. (5)) depends only on the DNNs' weights ($\boldsymbol{\Theta}_u$ and $\boldsymbol{\Theta}_\phi$) and the unknown model parameters K_c, K_η, and K_{Pe}. By minimizing the resulting $\mathscr{L}(\boldsymbol{\Theta}_u, \boldsymbol{\Theta}_\phi, K_c, K_\eta, K_{Pe})$ using $w_u = w_\phi = w_m = w_p = w_c = 1$, with respect to its arguments, we find suitable DNNs' weights and values of the parameters K_c, K_η, and K_{Pe} that simultaneously lead to the best agreement with the training data *and* the physics.

4.3.2   Comparison between PINN, theory and experiment

For Brownian suspensions, we substitute the parabolic velocity profile from Eq. (26) and the Brownian suspension viscosity from Eq. (29) into Eq. (21), to again obtain a nonlinear first-order ODE for $\phi(y^*)$:

$$\frac{d\phi}{dy^*} = \frac{2K_c \phi^2 \eta_r + 2y^* K_\eta \phi^2 f_2(\phi)}{(Pe^{-1} - 2K_c y^* \phi)\eta_r - 2y^* K_\eta \phi^2 f_1(\phi)}, \tag{32}$$

where

$$f_1(\phi) = \frac{d\eta_\infty}{d\phi} + \frac{d\eta_0/d\phi - d\eta_\infty/d\phi}{1 + K_{Pe} Pe \, y^*/(3\pi)},$$

$$= \frac{\mathfrak{a}_0}{\phi_{m_0}} \left(1 - \frac{\phi}{\phi_{m_0}} \right)^{-\mathfrak{a}_0 - 1} + \frac{(\mathfrak{a}_0/\phi_{m_0})(1 - \phi/\phi_{m_0})^{-\mathfrak{a}_0 - 1} - (\mathfrak{a}_\infty/\phi_{m_\infty})(1 - \phi/\phi_{m_\infty})^{-\mathfrak{a}_\infty - 1}}{1 + K_{Pe} Pe \, y^*/(3\pi)}, \tag{33a}$$

$$f_2(\phi) = -[\eta_0(\phi) - \eta_\infty(\phi)] \frac{K_{Pe} Pe/(3\pi)}{[1 + K_{Pe} Pe \, y^*/(3\pi)]^2}. \tag{33b}$$

Via the numerical procedure described in Sec. 4.2.2, we solve for the "theory" prediction for $\phi(y^*)$ from Eqs. (32) and (23), using the values for K_c and K_η in Eq. (32) and K_{Pe} in Eq. (33) obtain by PINN.

The comparisons between the experimental data of Frank et al. [50] (symbols), the theory (dashed), and the PINN (solid) are shown in Figs. 7 and 8. The comparisons show that the PINN predictions agree well
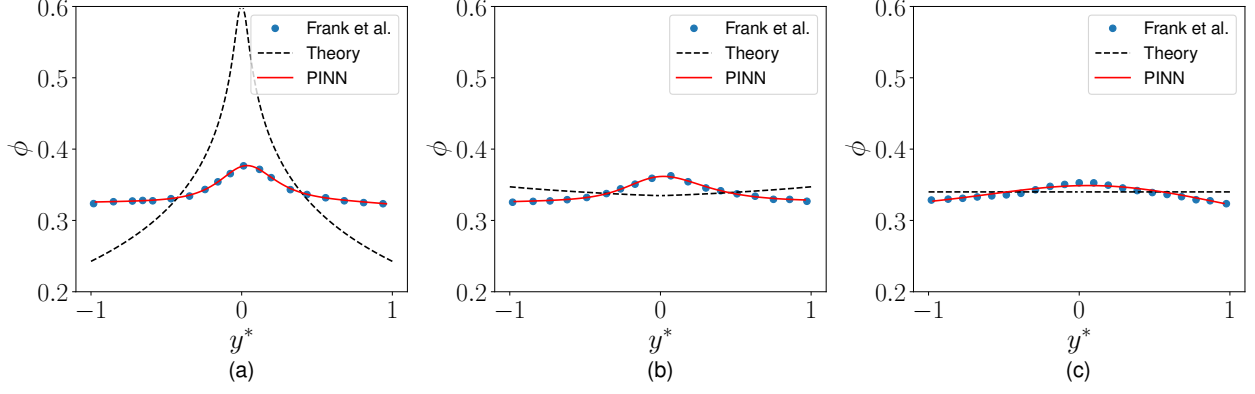
Figure 7: Application to experiment from Frank et al. [50] at $\phi_b = 0.34$: (a) $Pe = 4400$; (b) $Pe = 550$; (c) $Pe = 69$.
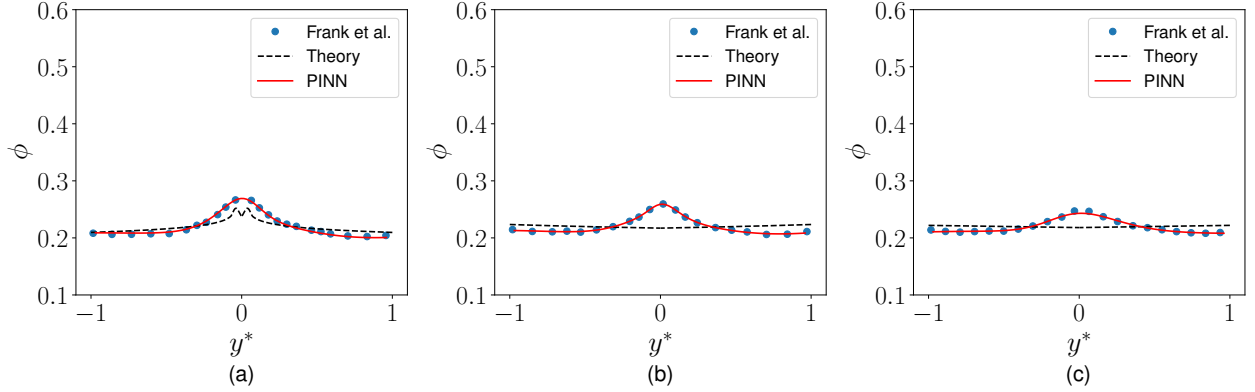

Figure 8: Application to experiment from Frank et al. [50] at $\phi_b = 0.22$: (a) $Pe = 4400$; (b) $Pe = 550$; (c) $Pe = 69$.

with experiment data, while the "theory" solutions do not. From discrete observations of u^* and ϕ from the experiments used as training data, the PINN algorithm not only accurately predicts the distributions of $u^*(y^*)$ and $\phi(y^*)$, but also "learns" the suitable values of K_c, K_η, and K_{Pe}, which were *a priori* unknown.

Table 2 summarizes the values that the PINN "learns" from experimental data with different values of ϕ_b and Pe. To account for the variations in the converged values of the unknown model parameters, due to the random initialization of the DNNs, we averaged the predictions from 100 initializations to obtain a statistical result with a mean and a standard error. Importantly, the PINN analysis suggests that K_c and K_η vary with ϕ_b and Pe. This critical issue was *not* addressed in previous works, in which the values of K_c and K_η are taken from [1] (validated only for the concentric Couette flow) and applied to any flow scenario. Now, however, we discover that K_η (in particular) decreases with Pe. In addition, we observe that the model is quite sensitive when applied to Brownian suspensions, with the standard error (from the 100 random DNN initializations) of the estimated values of K_c and K_η and K_{Pe} being comparable to the values of the parameters in some cases.

Interestingly, the result for $Pe = 69$ in Table 2 suggests that a vanishing viscosity-variation flux, $\|\mathbf{N}_\eta\| \approx 0$, for this Brownian case of $Pe \gg 1$. This result is consistent with the fact that the velocity profile is parabolic (recall Fig. 6), and the strongly-Brownian suspension effectively has the same viscosity as the Newtonian carrier fluid. Further, while the values obtained for K_{Pe} in Table 2 are on the same order as the value 1.31 used in literature, they are not the same, suggesting that this parameter (quantifying the suspension rheology's shear-dependence) should be measured for each experiment, if possible.

Note that the model from Eq. (32) breaks down if $d\phi/dy^*$ changes sign at some $y^* \neq 0$. This situation can occur when the denominator in Eq. (32) reaches 0. The $\phi(y^*)$ profile develops a seemingly nonphysical

ϕ_b	Pe	K_c	K_η	K_{Pe}
0.34	4400	$2.74 \times 10^{-4} \pm 2.23 \times 10^{-3}$	$8.28 \times 10^{-3} \pm 5.38 \times 10^{-2}$	$1.77 \pm 0.61 \times 10^{-1}$
0.34	550	$7.84 \times 10^{-5} \pm 4.64 \times 10^{-4}$	$6.32 \times 10^{-4} \pm 5.88 \times 10^{-3}$	$1.46 \pm 5.69 \times 10^{-1}$
0.34	69	$2.47 \times 10^{-4} \pm 3.92 \times 10^{-4}$	$3.58 \times 10^{-7} \pm 2.97 \times 10^{-6}$	$1.51 \pm 2.58 \times 10^{-2}$
0.22	4400	$4.17 \times 10^{-4} \pm 1.94 \times 10^{-3}$	$1.21 \times 10^{-2} \pm 7.37 \times 10^{-2}$	$1.71 \pm 4.85 \times 10^{-2}$
0.22	550	$9.98 \times 10^{-5} \pm 9.18 \times 10^{-4}$	$1.61 \times 10^{-3} \pm 1.39 \times 10^{-2}$	$1.47 \pm 1.69 \times 10^{-2}$
0.22	69	$5.73 \times 10^{-4} \pm 7.35 \times 10^{-4}$	$5.51 \times 10^{-7} \pm 7.12 \times 10^{-7}$	$1.51 \pm 1.07 \times 10^{-2}$

Table 2: Values of the shear-induced migration model's parameters K_c, K_η, and K_{Pe}, as inferred by the PINN from the experimental data of Frank et al. [50], for different bulk volume fractions ϕ_b and different values of shear Péclet number Pe. As before, these statistical results, with a mean and a standard error, come from 100 runs of the PINN algorithm using different random initializations of the NNs.

maximum on each side of the centerline $y^* = 0$ (see Fig. 7(b)). This observation highlights a deficiency of using the Phillips et al. [1] model for Brownian suspensions. Further, it is important to emphasize that this breakdown of the Brownian shear-induced migration model is unrelated to the fact that the shear rate vanishes at the center of the channel, which is a separate issue addressed by "nonlocal" shear rate modifications that account for non-continuum effects expected to arise at the scale of a single particle diameter [3, 10, 11]. On the other hand, the PINN approach predicts a smooth curve that agrees with the experimental data because the PINN does not attempt to interpret the model in a point-wise sense (or as a "law of nature," which it is clearly not), but rather the PINN only uses the model residual to constrain the learning process.

5   Conclusion

Thirty years later, the phenomenological model of Phillips et al. [1] continues to be the "workhorse" of macroscopic modeling of shear-induced particle migration in low-Reynolds-number flows of suspensions, as recent studies on simulation of migration in Brownian suspensions [17] and experiments [18] and simulations [19] on migration in complex fluids demonstrate. However, the model's parameters were only ever properly calibrated against experiments in an annular Couette cell [1]. Subsequent studies on shear-induced migration in Poiseuille flows [47, 50] showed that the model, as calibrated against the annular Couette flow data, is only in *qualitative* agreement with slot-flow experiments (despite being quantitatively accurate for Couette flow).

To remedy these apparent contradictions/difficulties exposed in the literature, we employed a machine learning methodology in which the model of Phillips et al. [1] is used constrain a machine learning approach to assimilating the experimental data on particle migration. Using the idea of physics-informed neural networks (PINNs) pioneered by Karnidakis and collaborators [22, 26], we constructed a loss function from the model of Phillips et al. [1] and optimized neural networks to simultaneously best-approximate velocity and volume fraction experimental data, as well as the unknown/phenomenological parameters of the model. The PINN approach seamlessly identified the unknown parameters as part of the training process. In doing so, we found that the parameter values calibrated against annular Couette flow experimental data are not accurate for other flow scenarios, such as Poiseuille flow and/or for a Brownian suspension. Additionally, the model's parameters were found to vary with the bulk volume fraction and the shear Péclet number of the suspension, which was previously not known. This point was particularly important for the case of Brownian suspensions, highlighting why the phenomenological model solved as "basic law" with the parameters from [1] (as done in [17]) could not match any of the experimental data.

In summary, we proposed to shift the paradigm of how phenomenological models for shear-induced migration should be used. The models widely used in the literature are only *post*dictive, requiring calibration against an experiment for each flow scenario they are to be used in. Even then, attempting to solve the models as a "basic law" to predict the particle distribution (having somehow best-fit the parameters) requires overcoming unphysical singularities. On the other hand, employing the models within the PINN approach does not require pointwise solutions or the parameters to be known *a priori*. Therefore, their values and, thus, the true relative importance of the different particle migration fluxes (collisional, viscosity-gradient

or Brownian) in a given experiment can be uncovered via PINNs (but not via the standard approach in the literature, based on directly solving an ODE for the particle distribution). It should be re-emphasized that using the parameter values (calibrated in 1992 only for annular Couette flow) in varied flow scenarios strongly enforces physics that *may or may not* be manifested in the particular flow under consideration. We have demonstrated that, to gain an understanding of the "unknown physics" (to use the terminology of Reyes et al. [31]) of particle migration in a variety of flow experiments, PINNs can be effectively employed to simultaneously solve the inverse and forward problems and to significantly extend the practical utility of the standard phenomenological models.

Acknowledgments

References

[1] R. J. Phillips, R. C. Armstrong, R. A. Brown, A. L. Graham, J. R. Abbott, A constitutive equation for concentrated suspensions that accounts for shear-induced particle migration, Phys. Fluids A 4 (1992) 30–40. doi:10.1063/1.858498.

[2] D. Leighton, A. Acrivos, The shear-induced migration of particles in concentrated suspensions, J. Fluid Mech. 181 (1987) 415–439. doi:10.1017/S0022112087002155.

[3] P. Mills, P. Snabre, Rheology and structure of concentrated suspensions of hard spheres. Shear induced particle migration, J. Physique II 5 (1995) 1597–1608. doi:10.1051/jp2:1995201.

[4] F. Gadala-Maria, A. Acrivos, Shear-induced structure in a concentrated suspension of solid spheres, J. Rheol. 24 (1980) 799–814. doi:10.1122/1.549584.

[5] J. J. Stickel, R. L. Powell, Fluid mechanics and rheology of dense suspensions, Ann. Rev. Fluid Mech. 37 (2005) 129–149. doi:10.1146/annurev.fluid.36.050802.122132.

[6] R. L. Panton, Incompressible flow, 4th ed., John Wiley & Sons, Hoboken, NJ, 2013. doi:10.1002/9781118713075.

[7] J. F. Morris, Toward a fluid mechanics of suspensions, Phys. Rev. Fluids 5 (2020) 110519. doi:10.1103/PhysRevFluids.5.110519.

[8] H. M. Vollebregt, R. G. M. Van Der Sman, R. M. Boom, Suspension flow modelling in particle migration and microfiltration, Soft Matter 6 (2010) 6052–6064. doi:10.1039/c0sm00217h.

[9] E. Guazzelli, J. F. Morris, A Physical Introduction to Suspension Dynamics, volume 45 of *Cambridge Texts in Applied Mathematics*, Cambridge University Press, New York, 2011. doi:10.1017/CBO9780511894671.

[10] P. R. Nott, J. F. Brady, Pressure-driven flow of suspensions: simulation and theory, J. Fluid Mech. 275 (1994) 157–199. doi:10.1017/S0022112094002326.

[11] J. F. Morris, F. Boulay, Curvilinear flows of noncolloidal suspensions: The role of normal stresses, J. Rheol. 43 (1999) 1213–1237. doi:10.1122/1.551021.

[12] R. M. Miller, J. F. Morris, Normal stress-driven migration and axial development in pressure-driven flow of concentrated suspensions, J. Non-Newtonian Fluid Mech. 135 (2006) 149–165. doi:10.1016/J.JNNFM.2005.11.009.

[13] D. Lhuillier, Migration of rigid particles in non-Brownian viscous suspensions, Phys. Fluids 21 (2009) 023302. doi:10.1063/1.3079672.

[14] P. R. Nott, E. Guazzelli, O. Pouliquen, The suspension balance model revisited, Phys. Fluids 23 (2011) 043304. doi:10.1063/1.3570921.

[15] F. Municchi, P. P. Nagrani, I. C. Christov, A two-fluid model for numerical simulation of shear-dominated suspension flows, Int. J. Multiphase Flow 120 (2019) 103079. doi:10.1016/j.ijmultiphaseflow.2019.07.015.

[16] M. Maxey, Simulation methods for particulate flows and concentrated suspensions, Annu. Rev. Fluid Mech. 49 (2017) 171–193. doi:10.1146/annurev-fluid-122414-034408.

[17] C. Kang, P. Mirbod, Shear-induced particle migration of semi-dilute and concentrated Brownian suspensions in both Poiseuille and circular Couette flow, Int. J. Multiphase Flow 126 (2020) 103239. doi:10.1016/j.ijmultiphaseflow.2020.103239.

[18] S. Fataei, E. Secrieru, V. Mechtcherine, Experimental Insights into Concrete Flow-Regimes Subject to Shear-Induced Particle Migration (SIPM) during Pumping, Materials 13 (2020) 1233. doi:10.3390/ma13051233.

[19] R. Hernández, Dynamics of concentrated suspensions in two-dimensional channel flow for non-Newtonian slurries, Int. J. Multiphase Flow (2021) 103616. doi:10.1016/j.ijmultiphaseflow.2021.103616.

[20] D. Merhi, E. Lemaire, G. Bossis, F. Moukalled, Particle migration in a concentrated suspension flowing between rotating parallel plates: Investigation of diffusion flux coefficients, J. Rheol. 49 (2005) 1429–1448. doi:10.1122/1.2079247.

[21] J. M. Bricker, J. E. Butler, Oscillatory shear of suspensions of noncolloidal particles, J. Rheol. 50 (2006) 711–728. doi:10.1122/1.2234366.

[22] M. Raissi, P. Perdikaris, G. Karniadakis, Physics-informed neural networks: A deep learning framework for solving forward and inverse problems involving nonlinear partial differential equations, J. Comput. Phys. 378 (2019) 686–707. doi:10.1016/j.jcp.2018.10.045.

[23] S. L. Brunton, J. N. Kutz, Data-Driven Science and Engineering, Cambridge University Press, Cambridge, UK, 2019. doi:10.1017/9781108380690.

[24] S. L. Brunton, B. R. Noack, P. Koumoutsakos, Machine Learning for Fluid Mechanics, Annu. Rev. Fluid Mech. 52 (2020) 477–508. doi:10.1146/annurev-fluid-010719-060214.

[25] M. P. Brenner, J. D. Eldredge, J. B. Freund, Perspective on machine learning for advancing fluid mechanics, Phys. Rev. Fluids 4 (2019) 100501. doi:10.1103/PhysRevFluids.4.100501.

[26] G. E. Karniadakis, I. G. Kevrekidis, L. Lu, P. Perdikaris, S. Wang, L. Yang, Physics-informed machine learning, Nat. Rev. Phys. 3 (2021) 422–440. doi:10.1038/s42254-021-00314-5.

[27] X. I. A. Yang, S. Zafar, J.-X. Wang, H. Xiao, Predictive large-eddy-simulation wall modeling via physics-informed neural networks, Phys. Rev. Fluids 4 (2019) 034602. doi:10.1103/PhysRevFluids.4.034602.

[28] Z. Mao, A. D. Jagtap, G. E. Karniadakis, Physics-informed neural networks for high-speed flows, Comput. Meth. Appl. Mech. Engng 360 (2020) 112789. doi:10.1016/j.cma.2019.112789.

[29] Q. He, A. M. Tartakovsky, Physics-Informed Neural Network Method for Forward and Backward Advection-Dispersion Equations, Water Res. Res. 57 (2021) e2020WR029479. doi:10.1029/2020WR029479.

[30] X. Jin, S. Cai, H. Li, G. E. Karniadakis, NSFnets (Navier-Stokes flow nets): Physics-informed neural networks for the incompressible Navier-Stokes equations, J. Comput. Phys. 426 (2021) 109951. doi:10.1016/j.jcp.2020.109951.

[31] B. Reyes, A. A. Howard, P. Perdikaris, A. M. Tartakovsky, Learning unknown physics of non-Newtonian fluids, Phys. Rev. Fluids 6 (2021) 073301. doi:10.1103/PhysRevFluids.6.073301.

[32] M. Raissi, A. Yazdani, G. E. Karniadakis, Hidden fluid mechanics: Learning velocity and pressure fields from flow visualizations, Science 367 (2020) 1026–1030. doi:10.1126/science.aaw4741.

[33] E. Haghighat, M. Raissi, A. Moure, H. Gomez, R. Juanes, A physics-informed deep learning framework for inversion and surrogate modeling in solid mechanics, Comput. Meth. Appl. Mech. Engng 379 (2021) 113741. doi:10.1016/j.cma.2021.113741.

[34] W. Li, M. Z. Bazant, J. Zhu, A physics-guided neural network framework for elastic plates: Comparison of governing equations-based and energy-based approaches, Comput. Meth. Appl. Mech. Engng 383 (2021) 113933. doi:10.1016/j.cma.2021.113933.

[35] E. Zhang, M. Yin, G. E. Karniadakis, Physics-Informed Neural Networks for Nonhomogeneous Material Identification in Elasticity Imaging, preprint (2020) arXiv:2009.04525.

[36] Y. Chen, L. Lu, G. E. Karniadakis, L. Dal Negro, Physics-informed neural networks for inverse problems in nano-optics and metamaterials, Optics Express 28 (2020) 11618. doi:10.1364/OE.384875.

[37] S. Cai, Z. Wang, S. Wang, P. Perdikaris, G. E. Karniadakis, Physics-Informed Neural Networks for Heat Transfer Problems, ASME J. Heat Transfer 143 (2021) 060801. doi:10.1115/1.4050542.

[38] A. G. Baydin, B. A. Pearlmutter, A. A. Radul, J. M. Siskind, Automatic Differentiation in Machine Learning: a Survey, J. Mach. Learning Res. 18 (2018) 1–43. URL: http://jmlr.org/papers/v18/17-468.html.

[39] X. Meng, G. E. Karniadakis, A composite neural network that learns from multi-fidelity data: Application to function approximation and inverse PDE problems, J. Comput. Phys. 401 (2020) 109020. doi:10.1016/j.jcp.2019.109020.

[40] S. Wang, X. Yu, P. Perdikaris, When and why PINNs fail to train: A neural tangent kernel perspective, J. Comput. Phys. (2021) 110768. doi:10.1016/j.jcp.2021.110768.

[41] M. Abadi, A. Agarwal, P. Barham, E. Brevdo, Z. Chen, C. Citro, G. S. Corrado, A. Davis, J. Dean, M. Devin, S. Ghemawat, I. Goodfellow, A. Harp, G. Irving, M. Isard, Y. Jia, R. Jozefowicz, L. Kaiser, M. Kudlur, K. Levenberg, D. Mané, R. Monga, S. Moore, D. Murray, C. Olah, M. Schuster, J. Shlens, B. Steiner, I. Sutskever, K. Talwar, P. Tucker, V. Vanhoucke, V. Vasudevan, F. Viégas, O. Vinyals, P. Warden, M. Wattenberg, M. Wicke, Y. Yu, X. Zheng, TensorFlow: Large-Scale Machine Learning on Heterogeneous Systems, 2015. URL: https://www.tensorflow.org/.

[42] D. P. Kingma, J. Ba, Adam: A Method for Stochastic Optimization, in: Y. Bengio, Y. LeCun (Eds.), 3rd International Conference on Learning Representations (ICLR), San Diego, CA, 2015. URL: http://arxiv.org/abs/1412.6980.

[43] I. M. Krieger, T. J. Dougherty, A Mechanism for Non-Newtonian Flow in Suspensions of Rigid Spheres, Trans. Soc. Rheol. 3 (1959) 137–152. doi:10.1122/1.548848.

[44] I. M. Krieger, Rheology of monodisperse latices, Adv. Colloid Interface Sci. 3 (1972) 111–136. doi:10.1016/0001-8686(72)80001-0.

[45] M. M. Denn, J. F. Morris, Rheology of non-Brownian suspensions, Ann. Rev. Chem. Biomolec. Eng. 5 (2014) 203–228. doi:10.1146/annurev-chembioeng-060713-040221.

[46] P. Virtanen, R. Gommers, T. E. Oliphant, M. Haberland, T. Reddy, D. Cournapeau, E. Burovski, P. Peterson, W. Weckesser, J. Bright, S. J. van der Walt, M. Brett, J. Wilson, K. J. Millman, N. Mayorov, A. R. J. Nelson, E. Jones, R. Kern, E. Larson, C. J. Carey, I. Polat, Y. Feng, E. W. Moore, J. VanderPlas, D. Laxalde, J. Perktold, R. Cimrman, I. Henriksen, E. A. Quintero, C. R. Harris, A. M. Archibald, A. H. Ribeiro, F. Pedregosa, P. van Mulbregt, SciPy 1.0: fundamental algorithms for scientific computing in Python, Nat. Methods 17 (2020) 261–272. doi:10.1038/s41592-019-0686-2.

[47] C. J. Koh, P. Hookham, L. G. Leal, An experimental investigation of concentrated suspension flows in a rectangular channel, J. Fluid Mech. 266 (1994) 1–32. doi:10.1017/S0022112094000911.

[48] S. C. Jana, B. Kapoor, A. Acrivos, Apparent wall slip velocity coefficients in concentrated suspensions of noncolloidal particles, J. Rheol. 39 (1995) 1123–1132. doi:10.1122/1.550631.

[49] D. M. Kalyon, Apparent slip and viscoplasticity of concentrated suspensions, J. Rheol. 49 (2005) 621–640. doi:10.1122/1.1879043.

[50] M. Frank, D. Anderson, E. R. Weeks, J. Morris, Particle migration in pressure-driven flow of a Brownian suspension, J. Fluid Mech. 493 (2003) 363–378. doi:10.1017/S0022112003006001.

[51] C. G. de Kruif, E. M. F. van Iersel, A. Vrij, W. B. Russel, Hard sphere colloidal dispersions: Viscosity as a function of shear rate and volume fraction, J. Chem. Phys. 83 (1985) 4717–4725. doi:10.1063/1.448997.

[52] A. Alwosheel, S. van Cranenburgh, C. G. Chorus, Is your dataset big enough? Sample size requirements when using artificial neural networks for discrete choice analysis, J. Choice Model. 28 (2018) 167–182. doi:10.1016/j.jocm.2018.07.002.

Appendix

A   Pre-processing of experimental data into training data

For training of the NNs, we utilize the experimental data from the literature. Specifically, we digitized the data from Fig. 7 of Ref. [1], Figs. 10, 11, 15, and 19 of Ref. [47], and Figs. 3 and 4 of Ref. [50]. Experimental data points in these figures are limited (approximately 20 points in each plot). The NNs need more data points to achieve successful training (approximately 50 times the number of weights [52]). Thus, assuming the particle migration profiles and suspension velocities are smooth functions, we use interpolation to generate more data samples for the training of the NNs from the limited experimental data points. Specifically, we use `interpolate.interp1d` from the SciPy stack in Python [46] to obtain values at sample points that are not part of the digitized experimental data.

B   Choice of number of hidden layers and neurons per layer

To attempt to find an optimal number of hidden layers and nodes per layer (and justify the choices made for the PINN architecture used in the main text), we plot the training error for different numbers of hidden layers, as shown in Fig. 9. We first train the PINNs for $10,000$ iterations using the "Adam" [42] optimizer, then we use the "L-BFGS-B" optimizer until convergence. Figure 9 shows that adding layers (and/or more neurons per layer) does not reduce the training error further, while this action leads to a significantly higher computational cost (and requires more computing resources for the training process to reach convergence). Fewer layers (and/or fewer neurons per layer) tends to lead to divergence, i.e., failure of the training process. Therefore, as a suitable trade-off, we use 2 hidden layers with 10 neurons in each layer in the NNs for PINN approach.
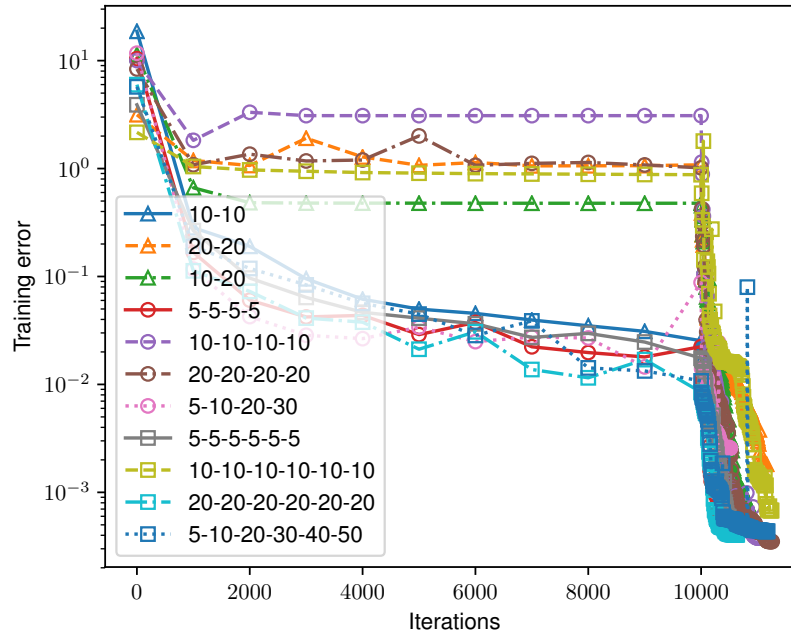

Figure 9: Training errors from PINNs with different numbers of hidden layers, and different number of neurons in each layer, in the NN architecture. The labels represent the layers and number of neurons per layer.